ARTICLES
https://doi.org/10.1038/s41560-019-0462-7

nature energy

Decoupled hydrogen and oxygen evolution by a two-step electrochemical–chemical cycle for efficient overall water splitting

Hen Dotan[1,5], Avigail Landman[2,5], Stafford W. Sheehan[1,3], Kirtiman Deo Malviya[1], Gennady E. Shter[4], Daniel A. Grave[1], Ziv Arzi[1], Nachshon Yehudai[4], Manar Halabi[4], Netta Gal[1], Noam Hadari[1], Coral Cohen[1], Avner Rothschild[1]* and Gideon S. Grader[4]*

Electrolytic hydrogen production faces technological challenges to improve its efficiency, economic value and potential for global integration. In conventional water electrolysis, the water oxidation and reduction reactions are coupled in both time and space, as they occur simultaneously at an anode and a cathode in the same cell. This introduces challenges, such as product separation, and sets strict constraints on material selection and process conditions. Here, we decouple these reactions by dividing the process into two steps: an electrochemical step that reduces water at the cathode and oxidizes the anode, followed by a spontaneous chemical step that is driven faster at higher temperature, which reduces the anode back to its initial state by oxidizing water. This enables overall water splitting at average cell voltages of 1.44–1.60 V with nominal current densities of 10–200 mA cm^{-2} in a membrane-free, two-electrode cell. This allows us to produce hydrogen at low voltages in a simple, cyclic process with high efficiency, robustness, safety and scale-up potential.

Clean energy utilization and its integration with an infrastructure built for energy storage and transportation requires effective fuel production. This helps to overcome the intermittency of solar and wind power and provides a high-energy-density fuel for transportation. To create such fuels in a sustainable manner, water oxidation is a critical step, utilized by the same photosynthetic organisms that we derive our fossil fuels from today[1]. This process oxidizes water to oxygen and liberates protons and electrons for fuel generation[2,3]. These can be used to produce carbon-based fuels by reducing carbon dioxide, or hydrogen by a more kinetically facile proton reduction. Beyond its ease of synthesis, hydrogen has further advantages over carbon-based fuels in its high energy density per unit mass, benign combustion by-products (H_2O) and potential to create synthetic feedstock chemicals downstream by proven and widely implemented technologies such as the Haber–Bosch process for ammonia production[4], or CO_2 hydrogenation to methane, methanol and other higher-order alkanes and alcohols[5].

In renewable processes for producing hydrogen, carbon-based fuels and ammonia, the reagent protons and electrons originate from the oxidation of water, with oxygen as a by-product[3]. In a purely electrolytic scheme, the water oxidation and reduction reactions are tightly coupled in both time and space, as they occur simultaneously at two electrodes—an anode and a cathode—placed together in the same cell[6]. This coupling introduces operational challenges, such as H_2/O_2 crossover at low current densities, which hampers operation under variable renewable energy sources such as solar and wind[7,8], and sets strict constraints on material selection and process conditions.

Following on previous work exploring different paths to decouple the water oxidation and reduction reactions[7–11], here we propose a method of decoupled water splitting that overcomes a substantial barrier to implementation; namely, the energy conversion efficiency. In doing so, we also provide more degrees of freedom in our scheme, enabling optimization of process parameters beyond conventional electrolysers[8]. We achieve this by dividing the water oxidation reaction into two steps: an electrochemical step that oxidizes the anode, followed by a spontaneous chemical step that reduces the anode back to its initial state by oxidizing water.

Electrochemical–chemical water splitting

The process we have developed is illustrated in Fig. 1, which compares alkaline water electrolysis (Fig. 1a) and our proposed process (Fig. 1b). The fuel formation reaction (hydrogen evolution in the case of water splitting) is unchanged in this scheme, since it occurs at the cathode, whereas our process only modifies the water oxidation reaction at the anode. Accordingly, in our process, water is reduced to hydrogen gas at the cathode, liberating OH^- ions. The four-electron oxygen evolution reaction (OER), which takes place at the anode in conventional electrolysis (Fig. 1a), is divided into two consecutive steps comprising four one-electron oxidation reactions of a nickel hydroxide ($Ni(OH)_2$) anode[12,13], followed by spontaneous oxygen evolution and anode regeneration in a thermally activated chemical step[14,15], as illustrated in Fig. 1b (see also Supplementary Note 1 and Supplementary Fig. 1 for more details).

Thus, in our two-step electrochemical–thermally activated chemical (E-TAC) cycle, the O–O bond is formed in the second step[16], when the oxidized anode (now nickel oxyhydroxide (NiOOH)) is reduced to $Ni(OH)_2$ in a spontaneous, exergonic chemical reaction that produces O_2 and regenerates the anode[17], completing the overall water-splitting reaction. Similarly to the

---

[1]Department of Materials Science and Engineering, Technion—Israel Institute of Technology, Haifa, Israel. [2]The Nancy and Stephen Grand Technion Energy Program, Technion—Israel Institute of Technology, Haifa, Israel. [3]Catalytic Innovations, Fall River, MA, USA. [4]Department of Chemical Engineering, Technion—Israel Institute of Technology, Haifa, Israel. [5]These authors contributed equally: Hen Dotan, Avigail Landman.
*e-mail: avner@mt.technion.ac.il; grader@technion.ac.il

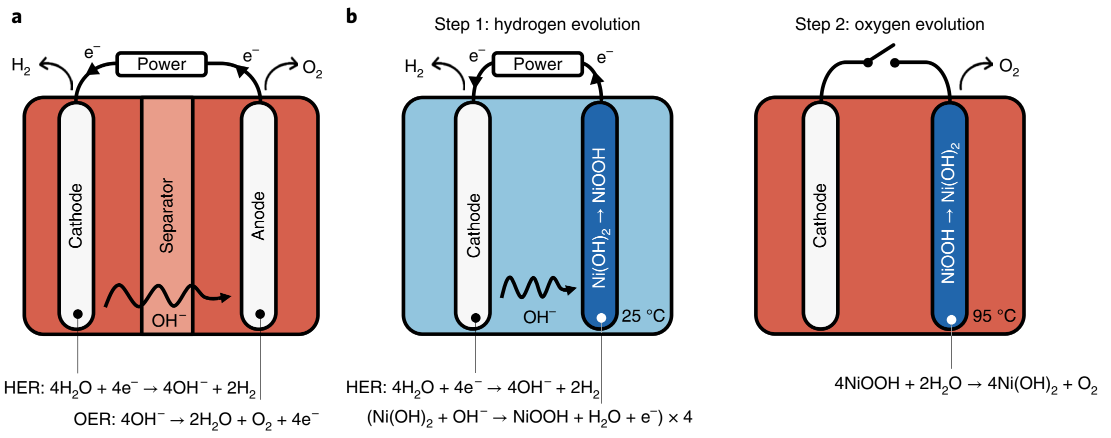

Fig. 1 | Schematic of alkaline water electrolysis and the E-TAC water-splitting process. a, In alkaline water electrolysis, which typically takes place at elevated temperatures (50–80 °C)[6], the OER and HER are coupled in both time and space, as they occur simultaneously at an anode and a cathode, which are placed together in the same cell. A diaphragm or anion exchange membrane separates the anode and cathode compartments and prevents O_2/H_2 crossover. **b**, E-TAC water splitting proceeds in two consecutive steps. An electrochemical step (left) reduces water by the conventional HER at the cathode, liberating hydroxide ions (OH^-) that oxidize a nickel hydroxide ($Ni(OH)_2$) anode into nickel oxyhydroxide (NiOOH). This step is followed by a chemical step (right), wherein the NiOOH anode reacts with water to spontaneously produce oxygen. The first (electrochemical) reaction occurs at ambient temperature (~25 °C), whereas the second (chemical) reaction proceeds at elevated temperatures (~95 °C) for the optimum rate of reaction. The first and second reactions sum up to the overall water-splitting reaction, $2H_2O \rightarrow 2H_2 + O_2$.

oxygen-evolving complex in natural systems[18], our scheme uses four metal centres to store oxidative equivalents, which helps to level the potential of the elementary oxidation reactions, thereby reducing the overall reaction overpotential[19]. Compared with previous work in this emerging field[8], our approach enables decoupled water splitting with enhanced efficiency and versatility, as shown below.

Electrode design

In brief, our E-TAC water-splitting process replaces the conventional water oxidation reaction in alkaline electrolysis with a two-step cycle in which the anode is first charged (electrochemically) and then regenerated (chemically). We emphasize that the hydrogen evolution reaction (HER) in the first step of our process remains the same as in alkaline electrolysis, except that it occurs at ambient temperature instead of elevated temperature (typically 50–80 °C)[6]. Therefore, the same cathode materials used in alkaline electrolysis, such as Raney nickel[6] or other HER catalysts, can be used in our process. In this work, we use platinized nickel-coated stainless-steel mesh cathodes as a standardized benchmark HER cathode for our proof-of-concept experiments.

The anode, which in our process functions in a completely different manner from conventional alkaline electrolysis, requires careful material selection and optimization. The key selection criteria for the anode include: stability in alkaline solutions; cyclability of the metal hydroxide and oxyhydroxide phases; a redox potential higher than the reversible OER potential (1.23 V_{RHE}) and lower than the potential at which oxygen evolves on the anode material (see Supplementary Note 1 for details); high capacity; fast charging and a fast rate of regeneration. These considerations all point to $Ni(OH)_2$/NiOOH anodes, which are commonly used in alkaline secondary batteries due to their cyclability and high energy density[20]. $Ni(OH)_2$ reversibly oxidizes to NiOOH according to the following reaction[12,13]: $Ni(OH)_2 + OH^- \leftrightarrow NiOOH + H_2O + e^-$.

Although the $Ni(OH)_2$/NiOOH standard redox potential is higher by 190 mV than the reversible OER potential, the OER is suppressed kinetically by its large overpotential. This enables alkaline batteries to operate thousands of cycles without parasitic oxygen evolution that leads to swelling and malfunction, as long as they are not overcharged. To suppress parasitic oxygen evolution that may occur on overcharging[21], additives that catalyse the $Ni(OH)_2$/NiOOH reaction and inhibit oxygen evolution are used[22–26]. One of the most commonly used additives is cobalt. Cobalt improves the electron and proton conductivity of the anode and shifts the $Ni(OH)_2$/NiOOH redox potential cathodically, expanding the potential window between charging and overcharging[27–30]. Therefore, $Ni_{1-x}Co_x(OH)_2$ anodes can be charged at a lower potential than their undoped $Ni(OH)_2$ counterparts, to a higher state of charge (SOC), without evolving oxygen.

Unlike battery anodes that should avoid oxygen generation, our anodes must generate oxygen in the second step of the E-TAC cycle. Additionally, it is essential to supress the spontaneous regeneration reaction, which is accompanied by oxygen evolution, during the hydrogen generation (first) step. Therefore, our anodes and operating conditions are tailored to suppress oxygen evolution in the first step and enhance oxygen generation in the second step (see Supplementary Notes 2–4 and Supplementary Figs. 2–13 for details). In this study, we use $Ni_{0.9}Co_{0.1}(OH)_2$ anodes, prepared by electrochemical impregnation (ECI) of nickel foam substrates (see Methods and Supplementary Figs. 2 and 3). ECI electrodes have a higher surface area than sintered or pasted electrodes, and can therefore sustain higher current densities at lower overpotentials[27–30]. Furthermore, the regeneration rate is much higher for the ECI anodes compared with their pasted counterparts (Supplementary Note 3). Optical and scanning electron microscope (SEM) micrographs, as well as X-ray diffractograms of the anodes are presented in Supplementary Figs. 14–24. These show conformal coating of the nickel foam substrate by a roughly 9-μm-thick layer of β-nickel hydroxide. The coating layer composition was determined by energy-dispersive spectroscopy, yielding an Ni:Co ratio of 6.7:1.0 (where $x \cong 0.1$; that is, $Ni_{0.9}Co_{0.1}(OH)_2$) (Supplementary Table 1).

Electrochemical characterization

The open-circuit potential (OCP) as a function of the SOC[27,31] and the cyclic voltammogram of a $Ni_{0.9}Co_{0.1}(OH)_2$ anode were measured and compared with those of an undoped $Ni(OH)_2$ anode (Supplementary Figs. 25 and 26). The OCP ranges from 1.31–1.41 V_{RHE} for the $Ni_{0.9}Co_{0.1}(OH)_2$ anode, and from 1.37–1.42 V_{RHE} for the undoped $Ni(OH)_2$ anode, over a SOC ranging from 10–90%.

The addition of cobalt shifts the potential cathodically by approximately 50 mV, suppressing oxygen evolution at the anode during the hydrogen generation step. The results reported hereafter were obtained with $Ni_{0.9}Co_{0.1}(OH)_2$ anodes.

The electrochemical properties of our $Ni_{0.9}Co_{0.1}(OH)_2$ anode were investigated, and compared with benchmark water oxidation catalyst NiFe layered double hydroxide (LDH). Cyclic voltammograms of the $Ni_{0.9}Co_{0.1}(OH)_2$ and NiFe LDH anodes are presented in Fig. 2a. The $Ni_{0.9}Co_{0.1}(OH)_2$ anode displays a large pseudo-capacitive oxidation wave of Ni^{+2} to Ni^{+3}, beginning at 1.3 V_{RHE} during the anodic sweep, preceding the water oxidation currents of both anodes. This shows the possibility to surpass the electrochemical efficiency of the NiFe LDH water oxidation catalyst.

To distinguish between the pseudo-capacitive anode oxidation current and the steady-state water oxidation current, chronoamperometry measurements were carried out at constant potentials between 1.3 and 1.7 V_{RHE} (Supplementary Fig. 27), as shown in Fig. 2b for 1.48 V_{RHE}. The asymptotic values obtained at different potentials yield the Tafel plot of the steady-state water oxidation current of both anodes, presented in Fig. 2c and overlaid in Fig. 2a (dotted curves). For the $Ni_{0.9}Co_{0.1}(OH)_2$ anode, the steady-state water oxidation current is much smaller than the pseudo-capacitive current measured in the cyclic voltammogram, indicating that the dominant process at these potentials is the pseudo-capacitive anode charging reaction. In contrast, when comparing steady-state water oxidation and pseudo-capacitive currents for the NiFe LDH anode, most of the net current arises from water oxidation.

Faradaic efficiency and H_2 gas purity

To determine the Faradaic efficiency of the $Ni_{0.9}Co_{0.1}(OH)_2$ anode charging reaction, we first compared the capacitive charge with the total charge that flows during chronoamperometric charging. On charging a fully discharged anode at a potential of 1.48 V_{RHE}, the Faradaic efficiency was larger than 99.7% for more than 2,000 s, during which the anode was charged by more than 50 C cm^{-2} (Supplementary Note 4 and Supplementary Fig. 27c). To verify that no oxygen was produced, the dissolved oxygen concentration in the electrolyte was monitored while charging a fully discharged anode at a constant potential of 1.48 V_{RHE}. No rise in the dissolved oxygen concentration was observed up to a charge of 55 C cm^{-2} (Supplementary Fig. 28).

The dissolved oxygen concentration was also monitored under conditions as similar as possible to the hydrogen generation step of the E-TAC process (see Methods) (that is, while charging the anode at a constant current). In addition, the dissolved oxygen concentration was also measured under chronoamperometric charging of a regenerated $Ni_{0.9}Co_{0.1}(OH)_2$ anode at 1.48 V_{RHE}. In both cases, no rise in the dissolved oxygen concentration above the background level was observed up to 3 C cm^{-2} (Supplementary Figs. 29 and 30), confirming that no oxygen was produced while charging the anode under these conditions. Finally, gas chromatography measurements displayed a rise in hydrogen concentration with no rise in the oxygen concentration in the headspace of a sealed cell on anode charging for 100 s at a constant current density of 50 mA cm^{-2} (that is, up to a charge of 5 C cm^{-2}) (Supplementary Fig. 31). These results confirm that no parasitic side reactions such as oxygen evolution take place while charging the anode during the hydrogen generation step of the E-TAC process.

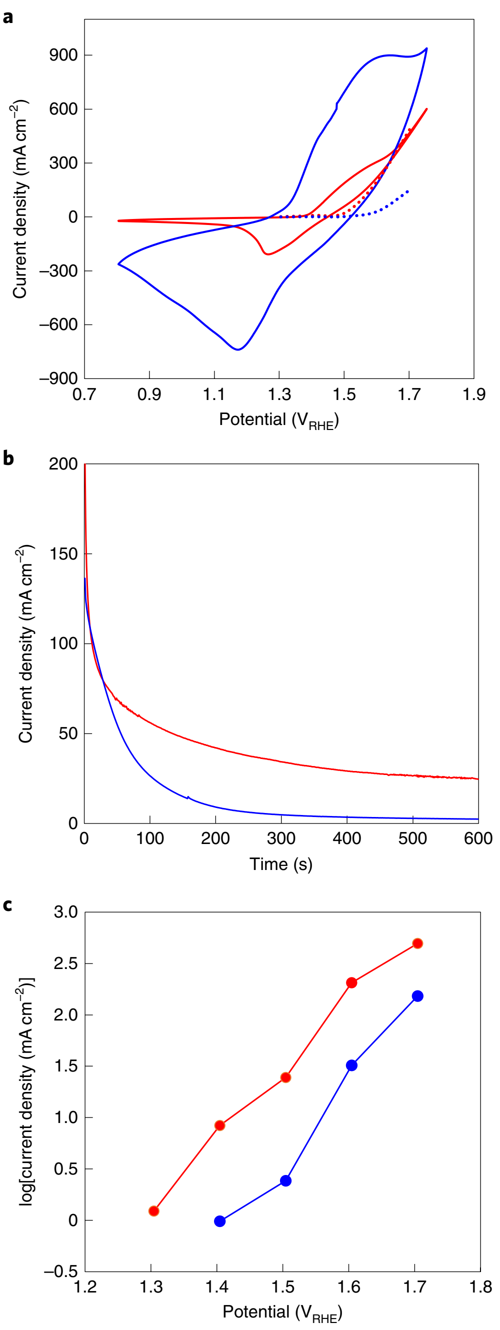

Fig. 2 | Electrochemical properties of $Ni_{0.9}Co_{0.1}(OH)_2$ and NiFe LDH anodes. a, Cyclic voltammograms measured at a scan rate of 50 mV s^{-1}. **b**, Chronoamperometric current traces at 1.48 V_{RHE}. **c**, Tafel plots of the steady-state water oxidation current as a function of the potential, from 10-min amperograms, such as those presented in **b**. The dotted curves in **a** represent the steady-state water oxidation current extracted from **c**. For all graphs, the $Ni_{0.9}Co_{0.1}(OH)_2$ anode is shown in blue and the NiFe LDH anode is shown in red. All tests were carried out in 5 M KOH at ambient temperature.

Proof of concept

In our proof-of-concept experiment, hydrogen was produced at the platinized nickel-coated stainless-steel cathode while the $Ni_{0.9}Co_{0.1}(OH)_2$ anode was oxidized to $Ni_{0.9}Co_{0.1}OOH$ in 5 M KOH aqueous solution (pH 15)[32,33]. A champion $Ni_{0.9}Co_{0.1}(OH)_2$ anode with a regenerated capacity of 5 C cm^{-2} was used. The hydrogen generation steps were carried out at ambient temperature (without heating or cooling) for 100 s at a current density of 50 mA cm^{-2}. We limited the applied cell voltage to not exceed the thermoneutral voltage (1.48 V) by more than 120 mV. This helped to minimize heat loss, and prevented oxygen generation and anode overcharging that may have transformed NiOOH from the β-phase to the γ-phase[20,22,34,35]. On the basis of the dissolved oxygen measurements

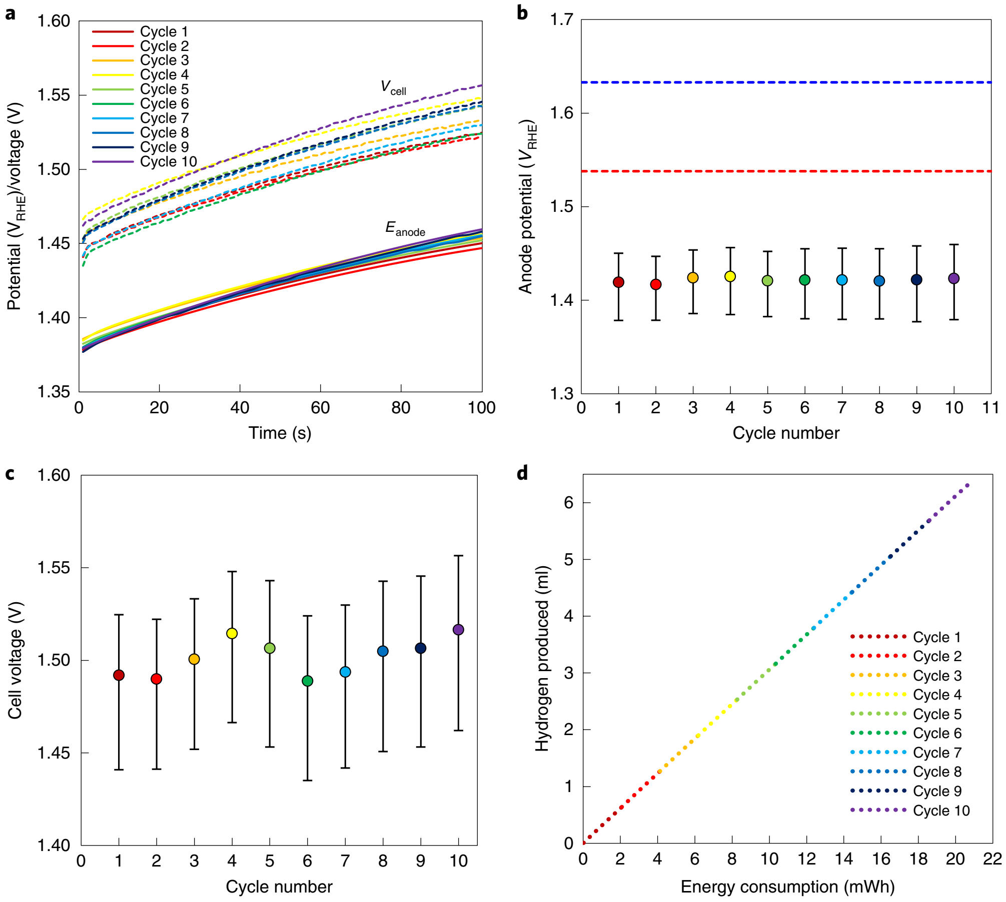

Fig. 3 | E-TAC water splitting in alkaline solution. a, Anode potential (E_{anode}, full lines) and cell voltage (V_{cell}, dashed lines) during the hydrogen generation steps of ten consecutive 100 s/100 s E-TAC cycles at a nominal current density of 50 mA cm^{-2} in 5 M KOH solution. **b**, Corresponding average anode potential (E_{anode}, data points) and range (bars) in each cycle. **c**, Average cell voltage (V_{cell}, data points) and range (bars) in each cycle. **d**, Cumulative hydrogen production (at 1 atm and 25 °C) as a function of electrical energy consumption during the E-TAC cycles. The blue and red dotted lines in **b** represent the potential of the OER reaction extracted from Fig. 2c at a steady-state current of 50 mA cm^{-2} of the $Ni_{0.9}Co_{0.1}(OH)_2$ anode and NiFe LDH anode, respectively. The cycle-to-cycle variations in the cell voltage in **a** are attributed to the cycling procedure that involved disconnecting and reconnecting the anode manually between the steps, leading to small variations in the contact and series resistances.

(Supplementary Fig. 30), the Faradaic efficiency of the anode charging reaction was 99.2% ± 0.1% for this amount of charge. The cell voltage, V_{cell}, and anode potential, E_{anode}, were recorded during the hydrogen generation (charging) steps and are presented in Fig. 3a.

After each of the 100-s hydrogen generation steps, the charged anode was taken out of the cold cell and placed in a hot (T = 95 °C) electrolyte (5 M KOH) for 100 s to accelerate spontaneous oxygen release and regeneration of its initial state. Significant bubble (O_2) formation was observed during the anode regeneration step, whereas during the hydrogen generation step, bubbles (H_2) were formed only on the cathode (Supplementary Videos 1 and 2).

The cell voltage and anode potential increased during each of the charging steps in a consistent manner, displaying little variability from cycle to cycle with no steady drift (Fig. 3a). This electrochemical behaviour indicates that the process is cyclable and proceeds without degradation; at the end of each cycle, the anode's SOC returns to its initial state with no measurable change. To confirm this, the anode cyclability was verified by ex situ microstructural (SEM) and crystallinity (X-ray powder diffraction) analyses before, during and after the E-TAC cycles (Supplementary Figs. 14–21).

During the hydrogen generation steps, the anode potential varied from 1.37–1.45 V_{RHE} (Fig. 3a)—well below the OER potential of both the $Ni_{0.9}Co_{0.1}(OH)_2$ and NiFe LDH anodes (presented by the blue and red dotted lines in Fig. 3b, respectively). At these potentials, oxygen evolution is negligible (Supplementary Figs. 27 and 30). The overall cell voltage varied from 1.44–1.56 V (Fig. 3a), with an average of 1.5 V for all ten cycles (Fig. 3c). The E-TAC process' voltage efficiency[36], V_{th}/V_{cell}, where V_{th} is the thermoneutral voltage of the water-splitting reaction (1.48 V under standard conditions), gave an average of 98.7% for all ten cycles. From the current × time product (that is, charge), one can calculate that 6.4 ml hydrogen (at 1 atm and 25 °C) was generated during the ten cycles presented in Fig. 3, consuming 20.8 mWh based on the current and cell voltage measured during the cycles, as shown in Fig. 3d. Therefore, the E-TAC process achieved a low electrical energy consumption of only 3.24 kWh m^{-3}, or 39.9 kWh kg^{-1} hydrogen.

In addition to the proof-of-concept experiment presented in Fig. 3, further tests were carried out to examine the efficiency and cyclability over a range of operational current densities and a large number of cycles. First, similar tests were carried out at different nominal current densities ranging from 10–200 mA cm^{-2}. The average cell voltage was found to increase from 1.44 V at 10 mA cm^{-2} to 1.60 V at 200 mA cm^{-2} (Supplementary Figs. 32 and 33). The anode potential in these tests was lower than that of the NiFe LDH benchmark anode (Supplementary Fig. 33), showing the higher electrochemical efficiency of our E-TAC approach compared with alkaline electrolysis with a state-of-the-art water

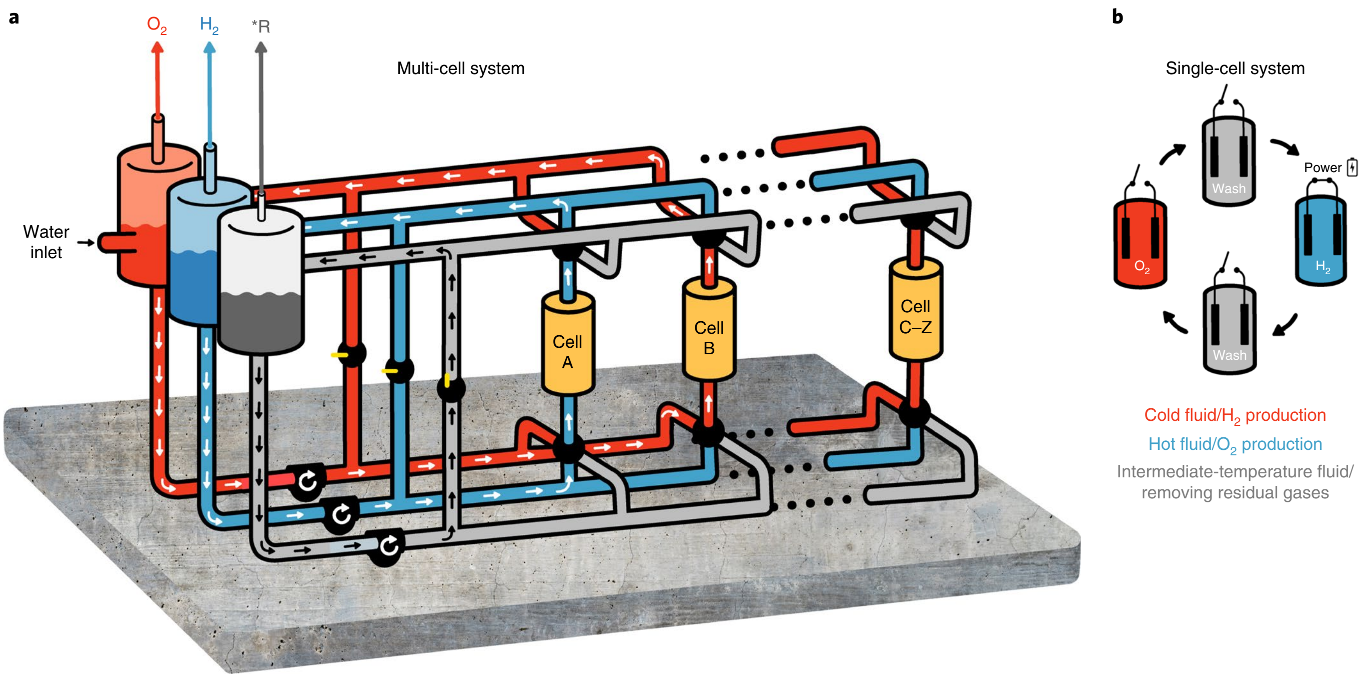

Fig. 4 | Schematic of the multi-cell E-TAC process. a, General electrolyte flow in the process, showing the cold electrolyte circulating in cell A, generating H_2 gas that is phase-separated in the middle (blue) tank on the left, while the hot electrolyte circulates in cell B, generating O_2 gas that is phase-separated in the red tank on the left. The intermediate-temperature wash fluid in the grey tank on the left is circulated through a bypass most of the time. This fluid is used to 'push' the cold and hot electrolyte solutions to their respective tanks at the end of the H_2 generation or O_2 generation steps. **b**, Single-cell cycle, showing the regenerative operation in each cell, where H_2 is generated under an electric bias at ambient temperature, and O_2 is generated at a hotter temperature without applying electric bias (open circuit). *R, residual gases.

oxidation catalyst. Second, 100 cycles were carried out at the same nominal current density as shown in Fig. 3 (50 mA cm^{-2}), providing evidence for stable, extended operation in alkaline solutions (Supplementary Fig. 34).

E-TAC water splitting in carbonate-buffered solutions

The proof-of-concept experiments presented so far were carried out in concentrated alkaline solution, which may be unsuitable for certain applications where highly caustic conditions cannot be tolerated. The option to decrease the solution pH to less hazardous levels is useful for low-cost implementation, due to the reduced balance of system costs that come with operation at extreme pH values and the potential for the use of low-purity water sources[37]. We thus demonstrate the versatility of our approach by also operating in a carbonate–bicarbonate (3:2 ratio of K_2CO_3:$KHCO_3$) buffer electrolyte with a pH of 10.6. In this test, the anode potential varied from 1.43–1.50 V_{RHE} at a nominal current density of 25 mA cm^{-2} (Supplementary Fig. 35). This shows that the E-TAC water-splitting process is not limited to alkaline solutions, with the potential to be applied more broadly in the electrochemical industry.

Proposal for scale-up and deployment

The results of our proof-of-concept experiment (Fig. 3) and the complementary tests presented in Supplementary Figs. 27–35 show the potential of the E-TAC water-splitting process to yield high electrochemical efficiency at a wide range of current densities with versatile operational conditions, while ensuring safe operation with no H_2/O_2 crossover. To transform these laboratory tests into an operational prototype system that produces pure hydrogen and oxygen gas streams, we envision a multi-cell system, as illustrated in Fig. 4a. Unlike the proof-of-concept tests presented above, this system contains stationary anodes and cathodes in each cell, operating in a swing configuration. During hydrogen production, a low-temperature electrolyte circulates through cell A, moving the hydrogen bubbles to the hydrogen separator (shown in blue). Simultaneously, a hot electrolyte flows through cell B to regenerate the (previously charged) anode, producing oxygen and moving the oxygen bubbles to the oxygen separator (shown in red). There are no moving electrodes in the entire system, simply hot and cold moving electrolyte solutions.

In addition to the hot and cold electrolytes, an intermediate-temperature fluid will be used to displace the cold (hot) electrolyte within each cell into the proper separation tank to avoid mixing of the hydrogen-saturated (oxygen-saturated) electrolyte with the hot (cold) electrolyte during the switch between cycle steps. The cycle that each single cell undergoes is illustrated in Fig. 4b, showing that between the cold and hot steps, the intermediate displacement fluid fills the cell. In addition, as shown in Fig. 1b, Fig. 4b shows that the electrodes are connected to a power source only during the hydrogen production step. The system will be hermetically sealed, so that high-purity hydrogen and oxygen streams are expected to be produced. In addition, the temporal separation of hydrogen and oxygen production in each cell adds a measure of safety to the proposed concept by reducing the potential for gas mixing. Finally, as shown in Fig. 4a, the system is envisioned to contain multiple cells, such that at any given point in time, some cells will be producing hydrogen, while the others produce oxygen.

Energy and heat balance

The results presented in Fig. 3 show only the electrical energy consumption during the first step of the E-TAC cycles, which is carried out at ambient temperature without heating. To accelerate the anode regeneration reaction on the second step, the anode is heated to 95 °C. This introduces some heat loss to the overall energy balance of our process, as discussed in detail in Supplementary Notes 5 and 6. However, since the first step in the E-TAC process is endo-

Table 1 | Comparison of different water-splitting schemes

Method	Operation mode	Membrane/ diaphragm	Current density (mA cm^{-2})	Average cell voltage (V)	Technology readiness level	Reference
			Decoupled watter splitting			
E-TAC	Swing	Not required	10	1.44	Research and development	This work
			50	1.50		
			100	1.56		
			200	1.60		
Solid-state redox mediator	Swap/swing	Not required	20	2.00	Research and development	10
			5	2.10	Research and development	11
Soluble electron-coupled proton buffers	Swing	PEM	100	2.94	Research and development	7
	Continuous		50	2.37	Research and development	9
Electrodeposition and dissolution	Swing	Not required	40	2.47	Commercial (Ergosup)	53
			60	2.75		
			Conventional (coupled) water splitting			
Alkaline electrolysis (NiFe LDH WOC)	Continuous	Diaphragm[a]	10	1.52	Research and development	54
Alkaline electrolysis (NiFe OOH WOC)		Diaphragm[a]	50	1.464		44
			500	1.586		
Alkaline electrolysis (zero gap)		AEM	200	1.5	Commercial (Hydrogenics)	55
Alkaline electrolysis (conventional)		Diaphragm	200–450	1.8–2.4	Commercial	6
PEM electrolysis (zero gap)		PEM	500–2,500	1.7–2.1	Commercial	6

[a]No diaphragm was employed in the reported tests. AEM, anion exchange membrane; WOC, water oxidation catalyst. Operating parameters and electrochemical efficiency (average cell voltage) are shown for landmark reports on decoupled water splitting, alkaline electrolysis with champion catalysts, commercial alkaline electrolysers and PEM electrolysers.

thermic for $V_{\text{cell}} < 1.56$ V (Supplementary Note 6), whereas the second step is exothermic (Supplementary Table 2), the heat loss that arises from swinging between the cold and hot steps can be minimized by careful heat management and thermal insulation of the hot components, and increasing the capacity of the anode so that the heat released during O_2 generation compensates for any other minor heat loss. We believe that this heat loss will add no more than 2 kWh kg^{-1} H_2 (Supplementary Note 6).

Advantages of the E-TAC approach

Our E-TAC process splits water in a membrane-free cell, generating hydrogen and oxygen in temporally separate steps. This yields several generic advantages of membraneless electrolysis compared with conventional water electrolysis, as reported elsewhere[38]. These include lower material and assembly costs, derived from reduced device complexity (Supplementary Note 7); lower maintenance costs; high tolerance to impurities in the electrolyte and adverse operating conditions, which typically foul membranes; and the opportunity to operate in non-hazardous buffer solutions, which also raises the operational safety while enabling the use of low-cost catalyst and/or construction materials. The problem of H_2/O_2 crossover across the membrane/separator in proton exchange membrane (PEM)/alkaline electrolysis[6,39,40] is avoided in our process, paving the path for partial-load water splitting[7,8] and high-pressure hydrogen production, as in the Ergosup hydrogen generator (https://www.ergosup.com/en/electrolysis-under-pressure).

Another key merit of the E-TAC process is its high efficiency. By tackling the four-electron OER using single-electron oxidation events of nickel hydroxide, and dividing water oxidation into separate one-electron electrochemical and thermally activated chemical steps, we are able to reduce the anode potential to a level competitive with the best reported water oxidation catalysts[31,41–45]. It is further noted that the efficiency of the E-TAC process is considerably higher than that of previous reports using the $Ni(OH)_2$/NiOOH redox couple as an auxiliary electrode to decouple the water oxidation and reduction reactions[10,11]. This is because, in our approach, oxygen is generated spontaneously by reacting $Ni(OH)_2$/NiOOH and water at our modified anodes, without the need for any electrode polarization from an external power source. In contrast, in previous reports[10,11] oxygen was generated electrochemically at a standard anode by polarizing the anode while the $Ni(OH)_2$/NiOOH auxiliary electrode discharged. Our anode design enables water permeation to NiOOH sites, and the inclusion of cobalt improves electron and proton conductivity while cathodically shifting the Ni^{+2}/Ni^{+3} redox potential, which enables this chemistry.

A similar approach that combines electrochemical and chemical reactions was presented previously[7]. It uses a molecular redox mediator that serves a similar role to the $Ni(OH)_2$/NiOOH anode in our scheme. Unlike the previous approach, which requires the use of an ion exchange membrane to prevent self-discharge, our use of a solid redox mediator (the $Ni(OH)_2$/NiOOH anode) prevents charged species from crossing between anode and cathode, thus eliminating the need for a membrane. Furthermore, the soluble redox mediator reported in ref. [7] operates in acidic solution, and therefore requires rare-Earth catalysts, such as platinum. In contrast, our solid redox mediator operates in alkaline solutions, enabling the use of low-cost, Earth-abundant catalysts. Lastly, our approach replaces the conventional water oxidation reaction, which has a higher overpotential than proton reduction, thereby yielding higher efficiency than in previous studies[7,9]. Table 1 compares the electrochemical efficiency (that is, the cell voltage) of our E-TAC process with other landmark reports on decoupled water splitting, as well as with alkaline electrolysis using champion catalysts, and commercial alkaline electrolysers and PEM electrolysers.

Currently, our anodes offer nominal current densities of up to 200 mA cm^{-2}, at the low end of commercial alkaline water electrolysers[6,40]. Achieving higher current densities requires further optimization using high-surface-area substrates and optimizing the anode fabrication process. It is noteworthy that indirect comparison between our anodes and electrolysis anodes is difficult because the E-TAC process occurs within the volume of the active $Ni_{0.9}Co_{0.1}(OH)_2$ layer, whereas in electrolysis, only the surface of the water oxidation catalyst participates in the reaction. Direct comparison with a benchmark water oxidation catalyst (NiFe LDH), using the same substrate and measurement conditions, shows that the operation potential of our anode is lower than that of the water oxidation catalyst (Fig. 3b).

Conclusion

With growing utilization of intermittent renewable electricity around the globe, efficient and viable ways of storing excess energy will become increasingly important. Our E-TAC process shows that water splitting at nearly thermoneutral conditions is indeed possible, and we emphasize the many avenues that can be explored to further optimize this process. Electrochemical properties and diffusion kinetics can be improved by design of optimized anode materials, as is shown here by the addition of cobalt. These anodes can be further engineered to tolerate high pressures for pressurized hydrogen production. This leads to applications for electromobility in transportation refuelling stations, chemical synthesis and energy storage when coupled with a fuel cell system. We also show that our approach is tolerant to carbonate-containing electrolytes at moderate pH values, which are significantly less hazardous than concentrated KOH solution. This, furthermore, leads to the potential for CO_2 reduction coupled with anode oxidation in a similar membrane-free cell, with an added benefit of enhanced product separation by spatially and temporally separating CO_2 reduction from oxygen generation[46]. Approaches like these open the door to electrolytic chemical production with efficient energy utilization[8].

Methods

Chemicals. Potassium hydroxide solutions were prepared using potassium hydroxide flakes (AR; Bio-Lab) in deionized water. Carbonate buffer solutions were prepared using potassium carbonate (minimum 99%; Spectrum) and potassium carbonate (99.5–101%; Sigma–Aldrich). Nitrate solutions for anode ECI were prepared using nickel nitrate powder (99.9+% Ni; Strem Chemicals), cobalt nitrate powder (≥98%; Sigma–Aldrich) and sodium nitrite powder (99.0%; Merck) in deionized water and ethanol (Ethanol ABS AR 99.9%; Gadot). The NiFe solutions were prepared using nickel nitrate powder and ferrous chloride (iron(II) chloride, 98%; Sigma–Aldrich).

$Ni_{0.9}Co_{0.1}(OH)_2$ anode fabrication. All $Ni_{0.9}Co_{0.1}(OH)_2$ anodes were prepared by ECI[27,47,48]. Nickel foam substrates (Ni-4753; RECEMAT; 3 mm thickness; 400-µm pores; 95.2% porosity; 5,400 m^2 m^{-3} specific surface) were cut into 1 cm × 2 cm pieces (Supplementary Fig. 2a). The substrates were dipped in acetone and ethanol, cleaned ultrasonically in isopropanol for 15 min, and then washed with deionized water. Before deposition, the substrates were vacuum immersed in the deposition solution for 30 min by placing the substrates in a vacuum chamber (Struers Epovac) and flooding them with the deposition solution. The deposition solution was composed of nickel nitrate, sodium nitrite and cobalt nitrate in an aqueous mixture of ethanol in water, titrated to an initial pH of 4 with nitric acid. A portion of 1 cm × 1 cm of each nickel foam substrate was dipped in the deposition solution, and the remaining portion was used as the electrical contact (Supplementary Fig. 2b). Each substrate was connected as the cathode to a potentiostat (SP-150 potentiostat (BioLogic Science Instruments) or Ivium-n-Stat multichannel Potentiostat/Galvanostat (Ivium Technologies)) and placed between two nickel foam pieces acting as anodes (Supplementary Fig. 3). Deposition was carried out at a constant temperature of 80 °C, by applying a cathodic current of 60 mA. After deposition, each electrode was washed thoroughly with deionized water, then aged in a 5 M KOH aqueous solution at 90 °C for 30 min. The proof-of-concept experiment presented in Fig. 3 was carried out using a champion $Ni_{0.9}Co_{0.1}(OH)_2$ anode with a regenerated charge of 5 C cm^{-2}. All other experiments were carried out with standard $Ni_{0.9}Co_{0.1}(OH)_2$ anodes with a regenerated charge of 3 C cm^{-2}. In addition, for comparison of the $Ni_{0.9}Co_{0.1}(OH)_2$ anodes with undoped $Ni(OH)_2$ (Supplementary Figs. 25 and 26), we prepared an undoped $Ni(OH)_2$ anode by the same process without cobalt nitrate.

NiFe LDH anode fabrication. The same nickel foam substrate described in the previous section was used for the fabrication of the NiFe LDH anode. The deposition solution comprised 0.095 M $Ni(NO_3)_2$ and 0.05 M $FeCl_2$ in deionized water. Before deposition, the solution was purged with N_2 gas for 20 min. The same cell configuration described in the previous section was also employed for NiFe LDH anode fabrication. Deposition was carried out by applying a pulsed cathodic current of 10 mA for 20 cycles of 2 s on/off pulses, following the methods described elsewhere[49]. Following deposition, the anode was washed in deionized water.

$Ni_{0.9}Co_{0.1}(OH)_2$ anode structural characterization. The microstructure, phase and elemental composition evolution of our $Ni_{0.9}Co_{0.1}(OH)_2$ anodes were examined by optical microscopy (using an Olympus BX51 optical microscope), scanning electron microscopy (using an FEI ESEM Quanta 200), energy-dispersive X-ray spectroscopy (using an Oxford Instruments EDS system) and X-ray diffraction (using a Rigaku SmartLab diffractometer), following different stages in the fabrication and operation processes (Supplementary Figs. 14–21 and Supplementary Table 1). To reduce cracking due to vacuum drying and shrinkage under the high-vacuum conditions (1.4×10^{-2} torr) in the SEM, the wet anodes were frozen before placing them inside the SEM. However, during SEM operation, the ice sublimed and cracks were formed. To show that the cracks observed in the SEM images of our anodes are drying shrinkage cracks that resulted from the high-vacuum conditions inside the SEM, optical microscopy imaging of wet anodes was carried out before, during and after SEM imaging (Supplementary Figs. 22–24).

Electrochemical characterization. The reversible potentials for anodes prepared with and without cobalt ($Ni_{0.9}Co_{0.1}(OH)_2$ and $Ni(OH)_2$, respectively) were measured as a function of their SOC. In this and all of the following electrochemical tests, each anode was connected as the working electrode to a potentiostat (Ivium-n-Stat multichannel Potentiostat/Galvanostat), with a nickel foil/foam counter electrode and an Hg/HgO/1 M NaOH reference electrode in 5 M KOH electrolyte at ambient temperature. Here, each anode was charged at a constant current density of 20 mA cm^{-2} to SOCs between 10 and 90%. At each SOC, the current was interrupted and the OCP was measured for 10,000 s, allowing adequate time for the interface between the anode and electrolyte to equilibrate. Then, the anode was discharged at the same current to SOCs between 90 and 10%, and at each point the current was interrupted and the OCP was measured again. The reversible potential at each SOC was calculated from OCP versus log[t] plots, based on the method described in refs. [50,51] (Supplementary Fig. 25). Following this experiment, the $Ni_{0.9}Co_{0.1}(OH)_2$ anode was charged using constant applied current densities of 10, 20, 50 and 100 mA cm^{-2} in the same cell to the same SOCs between 10 and 90%, and the polarization potentials were measured as a function of the SOC (Supplementary Fig. 25). Two additional similar anodes, with and without cobalt, were used to preform cyclic voltammetry sweeps at a scan rate of 50 mV s^{-1} (Supplementary Fig. 26).

Parameters affecting the anode regeneration reaction. A commercial nickel hydroxide battery anode (Batterix) was used to establish an efficient and reliable charge regeneration measurement technique. These tests were carried out in 1 M NaOH. The anode was charged at a constant current density of 10 mA cm^{-2} to a total charge of 5 mAh cm^{-2}, and its final polarization potential was recorded. Then, the anode was discharged at a constant current density of 5 mA cm^{-2} and recharged at 10 mA cm^{-2} to a total charge of 10 mAh cm^{-2}, and its polarization potential was recorded again. This was repeated in charging intervals of 5 mAh cm^{-2} up to a total charge of 25 mAh cm^{-2}. Next, the anode was discharged to the same charging points, and its discharging polarization potential was recorded at the end of each discharging step. This experiment was repeated three times (Supplementary Fig. 4). Then, two methods for evaluating the regenerated charge density, Q_{regen}, were examined (Supplementary Fig. 5). In the first method (method 1), the anode underwent cycles of charging → regeneration → discharging steps. First, the anode was discharged at a constant current density of 5 mA cm^{-2} to a cutoff potential of 1 V_{RHE}. Then, the anode was charged at a current density (j_{charge}) of 10 mA cm^{-2} to an accumulated charge density, $Q_{charge} = j_{charge} \times t$ of 20 mAh cm^{-2}. Next, the anode was regenerated by immersing it in 1 M NaOH aqueous solution at 80 °C for 32 min. Finally, the anode was discharged again at a constant current density ($j_{discharge}$) of 5 mA cm^{-2} to the same cutoff potential of 1 V_{RHE} while monitoring the transferred charge density, $Q_{discharge} = j_{discharge} \times t$. This cycle was repeated three times. In this method, the regenerated charge density was calculated as $Q_{regen} = Q_{charge} - Q_{discharge}$. In the second method (method 2), the anode was initially discharged under the same conditions, to the same cutoff potential of 1 V_{RHE}. Then, the anode was charged to a cumulated charge density of 20 mAh cm^{-2}, reaching a final polarization potential of 1.52 V_{RHE}. The final potential, $E_f = 1.52$ V_{RHE}, was thus correlated with the final charge density of 20 mAh cm^{-2}. Next, the anode was regenerated under the same conditions as in method 1, but unlike method 1, the anode was not discharged electrochemically following regeneration. This was repeated three times. In this method, the regenerated charge density was evaluated as: $Q_{\mathrm{regen}} = Q_{\mathrm{charge}}$.

The same commercial nickel hydroxide battery anode was used to investigate the effects of regeneration conditions on the regeneration process. The anode was charged at a constant current density of 5 mA cm^{-2} to a cutoff potential of 1.42 $\mathrm{V_{RHE}}$, then charged again at a constant potential of 1.42 $\mathrm{V_{RHE}}$ until a cutoff current density of 2.5 mA cm^{-2} was reached. Following this step, the anode was disconnected and placed in 5 M KOH electrolyte at different temperatures (T = 60, 70, 80 and 90 °C) for different time durations (t = 2, 4, 8, 16 and 32 min) to regenerate the active material. After each regeneration step, the anode was reconnected to the electrochemical cell and charged again. Q_{regen} was calculated according to method 2. This procedure was repeated five times at each data point (Supplementary Fig. 6).

A comparative performance assessment between a pasted commercial nickel hydroxide battery anode (Batterix) and our electrochemically impregnated $\mathrm{Ni_{0.9}Co_{0.1}(OH)_2}$ anode was carried out in 1 M NaOH by charging the anodes at current densities of 20, 50 and 100 mA cm^{-2} until cutoff potentials of 1.44, 1.46 and 1.52 $\mathrm{V_{RHE}}$, respectively, and then discharging them at a current density of 5 mA cm^{-2} until a cutoff potential of 0.92 $\mathrm{V_{RHE}}$. This was repeated three times for each current density (Supplementary Fig. 12).

Capacitive and Faradaic current measurements. A $\mathrm{Ni_{0.9}Co_{0.1}(OH)_2}$ anode and a NiFe LDH anode were compared according to the following. First, the anodes were subjected to cyclic voltammetry scans from 0.80–1.75 $\mathrm{V_{RHE}}$ at a scan rate of 50 mV s^{-1} (Fig. 2a). Then, the anodes were subjected to a series of chronoamperometric polarizations at potentials of 1.3–1.7 $\mathrm{V_{RHE}}$ at 100 mV intervals. Each polarization test was carried out for 600 s while monitoring the anode's current (Supplementary Fig. 27). The final current density was plotted against the polarization potential, and these Tafel plots are presented in Fig. 2c. The $\mathrm{Ni_{0.9}Co_{0.1}(OH)_2}$ anode was charged before the chronoamperometry tests to shorten the time required to reach the steady-state OER current. Finally, a fully discharged $\mathrm{Ni_{0.9}Co_{0.1}(OH)_2}$ anode was polarized at a constant potential of 1.48 $\mathrm{V_{RHE}}$ for 2,300 s to evaluate the Faradaic efficiency of the anode charging reaction at this potential (Supplementary Fig. 27).

Dissolved oxygen and gas chromatography measurements. For the dissolved oxygen measurements, a completely discharged $\mathrm{Ni_{0.9}Co_{0.1}(OH)_2}$ anode with a nominal active area of 10 cm^2 was placed in a hermetically sealed cell. The dissolved oxygen measurements were carried out in 0.5 M KOH solution (200 ml) at ambient temperature. A dissolved oxygen meter (Hanna Instruments; HI5421 DO/BOD/OUR/SOUR/Temperature Bench Meter) was submerged in the electrolyte. The pH was kept below 14 to avoid damaging the dissolved oxygen probe. The cell was purged with nitrogen gas ($\mathrm{N_2}$) for 30 min, followed by chronoamperometric polarization of the anode at a constant potential of 1.48 $\mathrm{V_{RHE}}$. The current and dissolved oxygen concentration were monitored during charging to 600 C (60 C cm^{-2}) with stirring (Supplementary Fig. 28).

To verify that no oxygen was produced during the hydrogen production step of the E-TAC cycle, the anode was subjected to E-TAC cycles with charging steps carried out at a constant current of 100 mA (10 mA cm^{-2}) until a cutoff charge of 30 C (3 C cm^{-2}), and the regeneration steps were carried out for 120 s in hot (95 °C) 5 M KOH solution (without the probe, so as not to damage it). The cycles were repeated until stabilization was reached. Then, the electrochemical cell was sealed and purged with nitrogen gas ($\mathrm{N_2}$) for 30 min with stirring. Finally, the anode was charged again at 100 mA for 30 C while the dissolved oxygen concentration was measured (Supplementary Fig. 29). It is noted that since the electrolyte solution was less concentrated (0.5 M KOH) than in the E-TAC tests (5 M KOH), the overpotential for the charging reaction was significantly higher than in the E-TAC tests. Therefore, the current density was set to 10 mA cm^{-2} to avoid reaching high potentials (>1.6 $\mathrm{V_{RHE}}$). As a control test, the same measurement was repeated with an uncoated nickel foam anode to perform water electrolysis at 100 mA (Supplementary Fig. 29). Following this test, the $\mathrm{Ni_{0.9}Co_{0.1}(OH)_2}$ anode was regenerated again in 5 M KOH solution at 95 °C for 120 s, then reconnected to the electrochemical cell. The cell was purged with $\mathrm{N_2}$ for 30 min, followed by chronoamperometric polarization of the anode at a constant potential of 1.48 $\mathrm{V_{RHE}}$. The current and dissolved oxygen concentration were measured for a total charge of 80 C (8 C cm^{-2}) (Supplementary Fig. 30).

For the gas chromatography measurements, an $\mathrm{Ni_{0.9}Co_{0.1}(OH)_2}$ anode with a nominal active area of 1 cm^2 was placed in a hermetically sealed cell. Before the measurement, the electrolyte was purged with $\mathrm{N_2}$ for 60 min, and a sample of 1 ml was extracted from the cell with a syringe and injected into sealed 20 ml vials that were pre-washed with $\mathrm{N_2}$. Then, a constant current of 50 mA (50 mA cm^{-2}) was applied between the electrodes for 100 s, as in the proof-of-concept test presented in Fig. 3, and another 1 ml sample was extracted from the headspace of the sealed cell and injected into a vial. A sample of 0.6 ml was taken from each vial and analysed by gas chromatography using an Agilent 7890A gas chromatography system (Supplementary Fig. 31).

E-TAC water-splitting tests in alkaline solution. A champion $\mathrm{Ni_{0.9}Co_{0.1}(OH)_2}$ anode with a regenerated charge of 5 C cm^{-2} was washed with deionized water and dried in a vacuum furnace at 40 °C until its weight stabilized. The anode's weight gain from the $\mathrm{Ni_{0.9}Co_{0.1}(OH)_2}$ coating was 0.26 g. To evaluate the anode's capacity, it was subjected to a series of charge/discharge cycles until its discharge capacity stabilized, yielding a capacity of 25 mAh cm^{-2} (90 C cm^{-2}). Before the E-TAC experiment presented in Fig. 3, the anode was completely discharged electrochemically at a current density of 5 mA cm^{-2}.

For the ten E-TAC cycles presented in Fig. 3, the anode was connected as the working electrode to a potentiostat (VersaSTAT 3; Princeton Applied Research) in a three-electrode configuration, with a 1 cm^2 platinized nickel-coated stainless-steel mesh counter electrode and an Hg/HgO/1 M NaOH reference electrode in 5 M KOH electrolyte at ambient temperature (without active heating or cooling). Additionally, an electrometer (Keithley 6514 System Electrometer) was used to measure the cell voltage (that is, the potential difference between the anode and the cathode). The cell was operated at a constant current density of 50 mA cm^{-2} (for both the anode and the cathode) for 100 s, charging the anode by 5 C cm^{-2}. Then, the charged anode was disconnected from the first cell and placed in another (second) cell filled with hot 5 M KOH electrolyte kept at a temperature of 95 °C by a thermostatic bath for 100 s. Then, it was taken out of the hot (second) cell and reconnected as the working electrode in the cold (first) electrochemical cell. Finally, the cell was operated again at 50 mA cm^{-2} for 100 s. This cycle was then repeated ten times, moving the anode from the cold cell to the hot cell and back to the cold cell.

The effect of the current density on the E-TAC process was examined by a series of E-TAC cycles carried out at different currents densities of 10, 25, 50, 100 and 200 mA cm^{-2} (Supplementary Fig. 32). The cell voltage and the potential of a $\mathrm{Ni_{0.9}Co_{0.1}(OH)_2}$ anode relative to an Hg/HgO/1 M NaOH reference electrode were measured simultaneously, using a standard anode with a regenerated charge of 3 C cm^{-2}. Before cycling, the cell was operated at a constant current density of 50 mA cm^{-2} until a cutoff potential of 1.43 $\mathrm{V_{RHE}}$ was reached. During each hydrogen generation step, a charge of 3 C was transferred to the anode. Then, the charged anode was disconnected and placed in a hot (95 °C) 5 M KOH electrolyte for 120 s for the regeneration step. This E-TAC cycle was repeated five times for each current density. The test at a current density of 200 mA cm^{-2} was carried out under slightly different conditions from the other tests. During the hydrogen generation step, the temperature was kept at 34 ± 2 °C, while the temperature of the oxygen generation step was elevated to 102 ± 2 °C.

The conversion to $\mathrm{V_{RHE}}$ from the raw data measured in $\mathrm{V_{Hg/HgO}}$ was done according to ref. [52]: $E^{\circ}_{\mathrm{Hg/HgO}}(T) = E^{\circ}_{\mathrm{Hg/HgO}}(298\,\mathrm{K}) - 1.120 \times 10^{-3} \times (T - 298) - 3.388 \times 10^{-6} \times (T - 298)^2$, where E° is the reversible potential.

Stability and cyclability tests. A (standard) $\mathrm{Ni_{0.9}Co_{0.1}(OH)_2}$ anode was initially charged at a constant current density of 50 mA cm^{-2} to a cutoff potential of 1.54 $\mathrm{V_{RHE}}$. Then, the anode was disconnected from the power source and placed in a hot (95 °C) 5 M KOH solution for 60 s for the TAC step. After 60 s, the anode was reconnected to the potentiostat, and the cell was operated at a current density of 50 mA cm^{-2} at the anode for 60 s (3 C cm^{-2}), or until the same cutoff potential of 1.54 $\mathrm{V_{RHE}}$ was reached. This cycle was repeated 100 times (Supplementary Fig. 34).

E-TAC water splitting in carbonate–bicarbonate electrolyte. A (standard) $\mathrm{Ni_{0.9}Co_{0.1}(OH)_2}$ anode was connected as the working electrode in a carbonate buffer solution containing 0.6 M $\mathrm{K_2CO_3}$ and 0.4 M $\mathrm{KHCO_3}$ (pH measured as 10.6) under ambient conditions. The cell was operated at a constant current density of 25 mA cm^{-2} for 100 s (2.5 C cm^{-2}) or until a cutoff potential of 1.53 $\mathrm{V_{RHE}}$ was reached. Then, the charged anode was disconnected and placed in a hot buffer solution containing 0.6 M $\mathrm{K_2CO_3}$ and 0.4 M $\mathrm{KHCO_3}$ kept at a temperature of 85–90 °C by a thermostatic bath for 100 s. At the end of the second step, the anode was taken out of the electrolyte and reconnected as the working electrode in the electrochemical cell, where it was operated again at a constant current density of 25 mA cm^{-2} for 100 s (2.5 C cm^{-2}). This procedure was repeated ten times to show stability during cycling (Supplementary Fig. 35).

Data availability

The data that support the plots within this paper and other findings of this study are available from the corresponding authors upon reasonable request.

Received: 19 January 2019; Accepted: 5 August 2019;

References

1. Barber, J. Photosystem II: the water splitting enzyme of photosynthesis and the origin of oxygen in our atmosphere. *Q. Rev. Biophys.* **49**, e14 (2016).
2. Hunter, B. M., Gray, H. B. & Muller, A. M. Earth-abundant heterogeneous water oxidation catalysts. *Chem. Rev.* **116**, 14120–14136 (2016).
3. Seh, Z. W. et al. Combining theory and experiment in electrocatalysis: insights into materials design. *Science* **355**, eaad4998 (2017).
4. Galloway, J. N. et al. Transformation of the nitrogen cycle: recent trends, questions, and potential solutions. *Science* **320**, 889–892 (2008).

5. Sheehan, S. W. et al. Commercializing solar fuels within today's markets. *Chem* **3**, 3–7 (2017).
6. Smolinka, T., Ojong, E. T. & Garche, J. in *Electrochemical Energy Storage for Renewable Sources and Grid Balancing* 103–128 (Elsevier, 2015).
7. Rausch, B., Symes, M. D., Chisholm, G. & Cronin, L. Decoupled catalytic hydrogen evolution from a molecular metal oxide redox mediator in water splitting. *Science* **345**, 1326–1330 (2014).
8. Wallace, A. G. & Symes, M. D. Decoupling strategies in electrochemical water splitting and beyond. *Joule* **2**, 1390–1395 (2018).
9. Symes, M. D. & Cronin, L. Decoupling hydrogen and oxygen evolution during electrolytic water splitting using an electron-coupled-proton buffer. *Nat. Chem.* **5**, 403–409 (2013).
10. Chen, L., Dong, X., Wang, Y. & Xia, Y. Separating hydrogen and oxygen evolution in alkaline water electrolysis using nickel hydroxide. *Nat. Commun.* **7**, 11741 (2016).
11. Landman, A. et al. Photoelectrochemical water splitting in separate oxygen and hydrogen cells. *Nat. Mater.* **16**, 646–651 (2017).
12. Bode, H., Witte, J. & Dehmelt, K. Zur kenntnis der nickelhydroxidelektrode—I. Uber das nickel (II)-hydroxidhydrat. *Electrochim. Acta* **11**, 1079–1087 (1966).
13. Bode, H., Witte, J. & Dehmelt, K. Zur kenntnis der nickelhydroxidelektrode. II. Über die oxydationsprodukte von nickel(II)-hydroxiden. *Z. Anorg. Allg. Chem.* **366**, 1–21 (1969).
14. Mao, Z. & White, R. E. The self-discharge of the $NiOOH/Ni(OH)_2$ electrode constant potential study. *J. Electrochem. Soc.* **139**, 1282–1289 (1992).
15. Winsel, A. & Fischer, C. New apparatus for the measurement of the self-discharge of the nickel hydroxide electrode. *J. Power Sources* **34**, 331–338 (1991).
16. Diaz-Morales, O., Ferrus-Suspedra, D. & Koper, M. T. M. The importance of nickel oxyhydroxide deprotonation on its activity towards electrochemical water oxidation. *Chem. Sci.* **7**, 2639–2645 (2016).
17. Macdonald, D. D. & Challingsworth, M. L. Thermodynamics of nickel-cadmium and nickel-hydrogen batteries. *J. Electrochem. Soc.* **140**, 606–609 (1993).
18. Cox, N. et al. Electronic structure of the oxygen-evolving complex in photosystem II prior to O–O bond formation. *Science* **345**, 804–808 (2014).
19. Dau, H. et al. The mechanism of water oxidation: from electrolysis via homogeneous to biological catalysis. *ChemCatChem* **2**, 724–761 (2010).
20. Mcbreen, J. in *Handbook of Battery Materials* (eds Daniel, C. & Besenhard, J. O.) 149–168 (Wiley-VCH, 2011).
21. Snook, Ga, Duffy, N. W. & Pandolfo, A. G. Evaluation of the effects of oxygen evolution on the capacity and cycle life of nickel hydroxide electrode materials. *J. Power Sources* **168**, 513–521 (2007).
22. Oliva, P., Laurent, J. F. & Leonardi, J. Review of the structure and the electrochemistry of nickel hydroxides and oxy-hydroxides. *J. Power Sources* **8**, 229–255 (1982).
23. Armstrong, R. D., Briggs, G. W. D. & Charles, E. A. Some effects of the addition of cobalt to the nickel hydroxide electrode. *J. Appl. Electrochem.* **18**, 215–219 (1988).
24. Ortiz, M. G., Castro, E. B. & Real, S. G. Effect of cobalt electroless deposition on nickel hydroxide electrodes. *Int. J. Hydrog. Energy* **39**, 6006–6012 (2014).
25. Wang, X. et al. Surface modification and electrochemical studies of spherical nickel hydroxide. *J. Power Sources* **72**, 221–225 (1998).
26. Wang, X., Luo, H., Yang, H., Sebastian, P. J. & Gamboa, S. A. Oxygen catalytic evolution reaction on nickel hydroxide electrode modified by electroless cobalt coating. *Int. J. Hydrog. Energy* **29**, 967–972 (2004).
27. Portemer, A., Delahaye-Vidal, A. & Figlarz, M. Characterization of active material deposited at the nickel hydroxide electrode by electrochemical impregnation. *J. Electrochem. Soc.* **139**, 671–678 (1992).
28. Johnson, B. A., Ferro, R. E., Swain, G. M. & Tatarchuk, B. T. High surface area, low-weight composite nickel fiber electrodes. *J. Power Sources* **47**, 251–259 (1994).
29. Ng, P. K. & Schneider, E. W. Distribution of nickel hydroxide in sintered nickel plaques measured by radiotracer method during electroimpregnation. *J. Electrochem. Soc.* **133**, 17–21 (1986).
30. Becker, M. D., Garaventta, G. N. & Visintin, A. Pulse-current electrodeposition for loading active material on nickel electrodes for rechargeable batteries. *ISRN Electrochem.* **2013**, 732815 (2013).
31. Jamesh, M. I. & Sun, X. Recent progress on Earth abundant electrocatalysts for oxygen evolution reaction (OER) in alkaline medium to achieve efficient water splitting—a review. *J. Power Sources* **400**, 31–68 (2018).
32. Meites, L. *Handbook of Analytical Chemistry* (McGraw-Hill, 1963).
33. Licht, S. pH measurement in concentrated alkaline solutions. *Anal. Chem.* **57**, 514–519 (1985).
34. Oshitani, M., Takayama, T., Takashima, K. & Tsuji, S. A study on the swelling of a sintered nickel hydroxide electrode. *J. Appl. Electrochem.* **16**, 403–412 (1986).
35. Chen, J., Bradhurst, D. H., Dou, S. X. & Liu, H. K. Nickel hydroxide as an active material for the positive electrode in rechargeable alkaline batteries. *J. Electrochem. Soc.* **146**, 3606–3612 (1999).
36. LeRoy, R. L. & Bowen, C. T. The thermodynamics of aqueous water electrolysis. *J. Electrochem. Soc.* **127**, 1954–1962 (1980).
37. Esswein, A. J., Surendranath, Y., Reece, S. Y. & Nocera, D. G. Highly active cobalt phosphate and borate based oxygen evolving catalysts operating in neutral and natural waters. *Energy Environ. Sci.* **4**, 499–504 (2011).
38. Esposito, D. V. Membraneless electrolyzers for low-cost hydrogen production in a renewable energy future. *Joule* **1**, 651–658 (2017).
39. Millet, P. in *Hydrogen Production:* Electrolysis (ed. Godula-Jopek, A.) 63–116 (Wiley-VCH, 2015).
40. Guillet, N. & Millet, P. in *Hydrogen Production: Electrolysis* (ed. Godula-Jopek, A.) 117–167 (Wiley-VCH, 2015).
41. Seitz, L. C. et al. A highly active and stable $IrO_x/SrIrO_3$ catalyst for the oxygen evolution reaction. *Science* **353**, 1011–1014 (2016).
42. Zhou, H. et al. Highly active catalyst derived from a 3D foam of $Fe(PO_3)_2/Ni_2P$ for extremely efficient water oxidation. *Proc. Natl Acad. Sci. USA* **114**, 5607–5611 (2017).
43. Dong, B. et al. Two-step synthesis of binary Ni–Fe sulfides supported on nickel foam as highly efficient electrocatalysts for the oxygen evolution reaction. *J. Mater. Chem. A* **4**, 13499–13508 (2016).
44. Zhou, H. et al. Water splitting by electrolysis at high current densities under 1.6 volts. *Energy Environ. Sci.* **11**, 2858–2864 (2018).
45. Han, L., Dong, S. & Wang, E. Transition-metal (Co, Ni, and Fe)-based electrocatalysts for the water oxidation reaction. *Adv. Mater.* **28**, 9266–9291 (2016).
46. Chen, C., Khosrowabadi Kotyk, J. F. & Sheehan, S. W. Progress toward commercial application of electrochemical carbon dioxide reduction. *Chem* **4**, 2571–2586 (2018).
47. Subbaiah, T., Mallick, S. C., Mishra, K. G., Sanjay, K. & Das, R. P. Electrochemical precipitation of nickel hydroxide. *J. Power Sources* **112**, 562–569 (2002).
48. Zhu, W., Zhang, D. & Ke, J. Electrochemical impregnation and performance of nickel hydroxide electrodes with porous plaques of hollow nickel fibres. *J. Power Sources* **56**, 157–164 (1995).
49. Batchellor, A. S. & Boettcher, S. W. Pulse-electrodeposited Ni–Fe (oxy) hydroxide oxygen evolution electrocatalysts with high geometric and intrinsic activities at large mass loadings. *ACS Catal.* **5**, 6680–6689 (2015).
50. Conway, B. E. & Bourgault, P. L. The electrochemical behavior of the nickel–nickel oxide electrode: part I. kinetics of self-discharge. *Can. J. Chem.* **37**, 292–307 (1959).
51. Barnard, R., Randell, C. F. & Tye, F. L. Studies concerning charged nickel hydroxide electrodes. I. Measurement of reversible potentials. *J. Appl. Electrochem.* **10**, 109–125 (1980).
52. Nickell, R. A., Zhu, W. H., Payne, R. U., Cahela, D. R. & Tatarchuk, B. J. Hg/HgO electrode and hydrogen evolution potentials in aqueous sodium hydroxide. *J. Power Sources* **161**, 1217–1224 (2006).
53. Bienvenu, G. Method for co-generation of electric energy and hydrogen. US patent 8,617,766 (2013).
54. Chen, G. et al. Accelerated hydrogen evolution kinetics on NiFe-layered double hydroxide electrocatalysts by tailoring water dissociation active sites. *Adv. Mater.* **30**, 1706279 (2018).
55. Pletcher, D. & Li, X. Prospects for alkaline zero gap water electrolysers for hydrogen production. *Int. J. Hydrog. Energy* **36**, 15089–15104 (2011).

Acknowledgements

The research leading to these results has received funding from the Israeli Ministry of National Infrastructure, Energy and Water Resources, as well as the European Research Council under the European Union's Horizon 2020 research and innovation programme (grant agreement number 727606). The results were obtained using central facilities at Technion's Hydrogen Technologies Research Laboratory, created and supported by the Nancy and Stephen Grand Technion Energy Program and the Adelis Foundation, and at the N_2–H_2 alternative fuel laboratory donated by Ed Satell. G.S.G. also acknowledges the support of the Arturo Gruenbaum Chair in Material Engineering. The authors thank Y. Ein-Eli for reading the manuscript and providing useful suggestions for improving it, and N. Haimovich for some of the heat balance calculations.

Author contributions

H.D. conceived the conceptual idea. H.D. and A.L. designed the experiments and analysed the data. A.L. performed the main experiment presented in Fig. 4 of the article, and most of the experiments presented in the Supplementary Information. S.W.S. designed and performed the experiments presented in Fig. 3 of the article, and tested alternative electrolyte solutions. K.D.M., A.L., M.H., N.Y. and C.C. prepared the electrodes. K.D.M., H.D. and D.A.G. performed the material characterizations. Z.A., N.Y., N.G. and N.H. performed the complementary experiments presented in the Supplementary Information. G.E.S. assisted in the experimental and system design. A.R.,

G.S.G., A.L., H.D., S.W.S. and D.A.G. wrote the manuscript. A.R. and G.S.G. supervised and guided the entire project.

Competing interests

H.D., A.L., G.E.S., A.R. and G.S.G. hold the following patent applications in relation to the E-TAC process and systems: Patent Cooperation Treaty international applications EP3221493A1, WO2016079746A1, US20170306510A1 and JP2017526564A (2015), and Israeli Patent Application number 258252 (2018). The above authors hold shares in H2Pro—a start-up company that aims to develop hydrogen generators based on the E-TAC process.

Additional information

Supplementary information is available for this paper at https://doi.org/10.1038/s41560-019-0462-7.

Reprints and permissions information is available at www.nature.com/reprints.

Correspondence and requests for materials should be addressed to A.R. or G.S.G.